

Scalable Printing of High-Resolution Flexible Transparent Grid Electrodes Using Directed Assembly of Silver Nanoparticles

Salman A. Abbasi, Zhimin Chai, and Ahmed Busnaina*

Next-generation optoelectronic applications such as virtual and augmented reality systems need ultrahigh resolution displays with a greater number of smaller, tightly packed pixels to avoid issues such as aliasing and the screen-door effect. High-resolution grid electrodes with submicron or nanoscale line widths are ideal for successful integration of more pixels with smaller light-emitting diodes. Solution-printed metal grid electrodes are a cost-effective alternative to the vapor-deposited indium tin oxide or metal grid transparent electrodes, but a scalable method to print high-resolution ($\leq 2 \mu\text{m}$ line width) grid structures over large flexible or rigid substrates remains elusive. A versatile, scalable, directed assembly process is presented for printing high-resolution grid transparent conductive electrodes under ambient conditions using silver nanoparticles over large substrates. Silver grid electrodes with line widths of $2 \mu\text{m}$ and 300 nm are printed using the described process. The aspect ratio and hence the electrical properties of the transparent electrodes are tailored using the withdrawal speed and the depth of the patterned photoresist. A high-performance grid electrode with a sheet resistance of $43 \Omega \text{ sq}^{-1}$ and an average transmittance of $\approx 93\%$ to visible light is realized. The printed grid electrodes are also remarkably flexible and are suited to a wide variety of conventional and emerging optoelectronic applications.

Metal grid electrodes have emerged as a flexible and cost-effective alternative to indium tin oxide (ITO) as transparent conductive electrodes (TCEs) for optoelectronic devices such as touch screens,^[1] liquid crystal displays,^[2] solar cells^[3] and light-emitting diodes (OLEDs).^[4] Grid TCEs provide good conductivity, flexibility and high optical transmittance, potentially at a low cost. The transparency and conductivity of metal grid electrodes can be tailored by tuning the grid's line width, thickness and pitch. Previously, grid electrodes have been developed using both vapor deposition and solution-based methods using patterning techniques such as electron beam lithography (EBL),^[5] photolithography,^[6] and nanoimprint lithography.^[7] For some emerging applications, decreasing the line width of grid electrodes to the limit of photolithography and possibly below

that is required. Smaller line widths provide increased transparency to visible light without decreasing the conductivity or the density of the grid. For next-generation optoelectronic applications such as displays for virtual and augmented reality, smaller, densely packed LEDs are needed to eliminate nuisances such as the screen-door effect,^[8] in which the unlit region between pixels is visible to the user. To operate such smaller LEDs, one requirement is grid electrodes with a line width of less than or equal to the size of the LED pixel for maximum optical transmittance. Moreover, decreasing line widths may reduce shadow loss in solar panels thereby increasing their efficiency.^[3] Therefore, there is strong impetus to make grid electrodes with submicron and nanoscale line widths. While vapor deposition methods can deliver high-resolution electrodes with excellent electrical properties, they are costly because of being subtractive and requiring high vacuum. Moreover, vapor deposition methods are particularly challenging to employ with

large, flexible substrates needed for emerging lighting and solar cell applications. Solution-based methods such as inkjet printing,^[9] ink evaporation,^[10] spin casting,^[11] doctor-blading/coating,^[12] UV embossing,^[13] femtosecond laser printing,^[14] vacuum filtration,^[15] electrohydrodynamic jet printing,^[16] microcontact printing,^[17] and transfer printing^[18] have thus been used to create metal grid electrodes. While most solution-based methods do not require high temperatures/pressures, they are either subtractive or non-scalable as some methods involve nonselectively coating the entire substrate with ink followed by the removal of excess. Nanoparticle inks are expensive and have a high-embodied energy,^[19] which makes subtractive printing processes less viable for mass production as wastage of ink for such processes is unavoidable. The most significant technical drawback of solution-based methods, however, is the inability to provide line widths of less than $\approx 10 \mu\text{m}$ on large substrates (inch scale) desirable for many emerging applications. Hence, there is need for a cost-effective and scalable solution-based method to selectively make high-resolution structures ($\ll 10 \mu\text{m}$) over large substrates. To the best of our knowledge, the highest resolution demonstrated by solution-based processes for grid structures over large areas (inch scale) is $\approx 5 \mu\text{m}$ using a combination of electrohydrodynamic jet and transfer printing.^[20] A proprietary process by Suzhou NanoGrid

S. A. Abbasi, Dr. Z. Chai, Prof. A. Busnaina
NSF Center for Nanoscale Science and High-Rate Nanomanufacturing
Northeastern University
Boston, MA 02115, USA
E-mail: busnaina@coe.neu.edu

The ORCID identification number(s) for the author(s) of this article can be found under <https://doi.org/10.1002/admi.201900898>.

DOI: 10.1002/admi.201900898

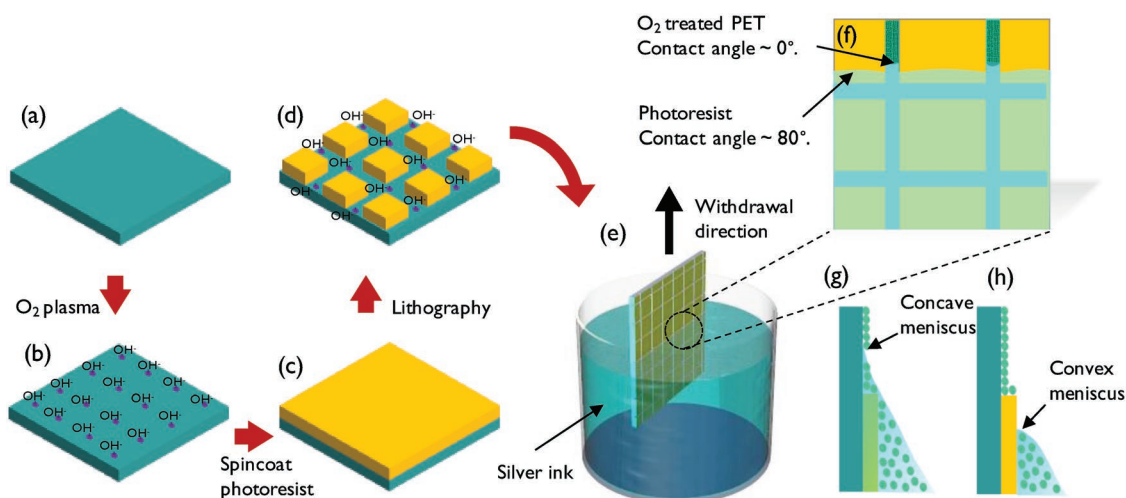


Figure 1. Sample preparation steps are summarized in (a)–(d). The dipcoating-based printing process is demonstrated in (e) while the mechanism based on the difference in wettability of the PET and the photoresist is visually explained in (f)–(h).

Ltd. claims to print grids down to 3 μm by pushing a nanoparticle paste into trenches with a doctor blade. Our study, however, demonstrates grid electrodes with submicron line widths using a facile directed-assembly-based method to selectively print silver-based grid electrodes on lithographically patterned transparent substrates. First, the process for printing grid electrodes with 2 μm line width and 100 μm pitch on a 5 cm \times 5 cm flexible poly(ethylene terephthalate) (PET) substrate is described. The capability of the proposed process to print a grid electrode with nanoscale line width (300 nm) is also demonstrated on glass.

The process starts by treating the PET substrate with oxygen (O₂) plasma to clean its surface and make it highly hydrophilic (contact angle $\approx 0^\circ$ with respect to deionized water). The substrate was then patterned with a grid pattern using photolithography with 2 μm line width and 100 μm pitch. The choice of the photoresist is used to control the depth of the patterned grid. In this study, two different photoresist thicknesses, ≈ 0.6 μm thick (Microposit S1805) and 1.3 μm thick (Microposit S1813), were used to create grid patterns using UV lithography. The sample preparation is described in more detail in the experimental section. Postpatterning, the contact angle of water on the photoresist was 68°, which increased to nearly 80° after hard-baking the patterned PET substrate at 115 °C on the hotplate for 2 min. After preparing the PET sample, a directed assembly-based printing process was employed using a 2 wt% aqueous silver ink as shown in **Figure 1**. Each patterned substrate was lowered vertically into a tank containing silver ink and withdrawn at a fixed speed using a dipcoater. The withdrawal speed was varied between 0.25 and 1 mm min⁻¹ (0.25, 0.5, 0.75, and 1 mm min⁻¹) for samples prepared with both thin and thick photoresists (0.6 and 1.3 μm) to characterize the effect of a) the thickness of the patterned grid, and b) the withdrawal speed, on the electrical properties of the printed transparent electrodes. Both parameters are linked to the thickness and density of the printed silver lines as demonstrated later. The dipcoating-based printing process used herein exploits the preferential wettability of the plasma-treated PET substrate achieved by a photoresist

template. Depending on the withdrawal speed, the dipcoating process operates in either evaporative or draining regime, the physics of which are described elsewhere.^[21] The nature of the fluid/air interface, defined by the surface tension of the liquid and the surface energy of the solid, plays an important role in the assembly process.^[22] For slower withdrawal speeds as is the case for this study, evaporative regime is dominant, and the thickness of the deposited/assembly film decreases with increasing withdrawal speed. In the evaporative regime, capillary flow wicks the ink into the thin patterned channels and assembly takes place due to the evaporation of the solvent at the solid/liquid interface. During assembly, capillary force causes the ink meniscus to spread and readily wet the exposed, highly hydrophilic O₂ plasma-treated, PET surface while the spreading of ink on the photoresist is suppressed due to its low surface energy as depicted in **Figure 1f–h**. This difference in the wetting behavior of the meniscus at the air/ink/substrate interface causes the liquid in the ink to evaporate faster at the meniscus on the PET surface than the photoresist surface. As the solvent evaporates at the meniscus, the evaporated volume is replenished by convective flow from the bulk of the suspension that brings along suspended particles. The evaporation of the liquid at the meniscus leaves behind the suspended silver particles assembled in patterned grid lines.^[23] Because the ink does not spread readily on the photoresist surface and the evaporation rate is slow, few particles are deposited on the photoresist surface compared to the patterned PET lines. Our group has previously demonstrated photoresist templating for printing carbon nanotubes.^[24]

After the assembly process, silver pads were deposited using electron beam evaporation to aid electrical characterization as shown in **Figure S1** (Supporting Information). Following metal deposition, the samples were first sintered on a hotplate at 150 °C for 20 min before its sheet resistance was measured. Flash annealing, using a xenon lamp with a 200–1000 nm wavelength, was then used to sinter the samples and the sheet resistance was characterized, again. This method, called flash or photonic sintering, is particularly attractive for flexible

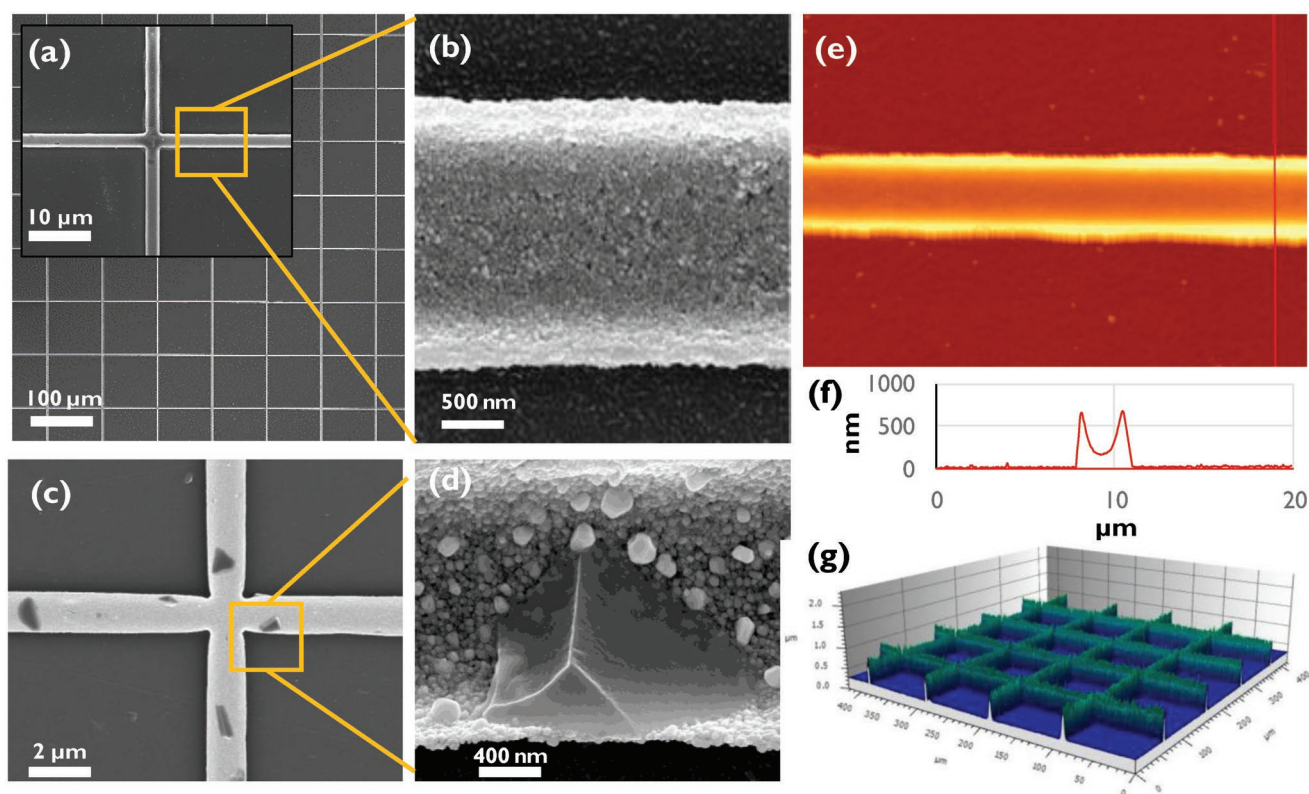


Figure 2. SEM micrographs of the printed grid ($1.3 \mu\text{m}$ thick photoresist, 0.5 mm min^{-1}) after hotplate sintering are shown in (a) and (b). The same sample after flash sintering is shown in (c) and (d) and the dark areas in (c) show silver crystals. AFM micrograph of a printed silver line (hotplate sintered) is shown in (e) and the extracted cross-sectional profile is shown in (f). A large area 3D-projection captured with a confocal microscope is shown in (g).

substrates as it can heat the surface of a substrate without significantly affecting its bulk. Scanning electron microscopy (SEM) was used to study the morphology of the printed silver grid after each sintering process. Atomic force microscopy (AFM) and confocal microscopy were used to ascertain the profile and the average thicknesses of the printed silver lines, respectively. The printed grid along with the SEM, AFM, and confocal microscopy micrographs of printed silver is shown in **Figure 2**. Particles coalesce, and large silver crystals form after flash sintering as shown in **Figure 2c,d**, which increases the conductivity of the printed electrode. AFM measurements revealed a concave profile of the printed lines as shown in **Figure 2**. This manifests the coffee ring effect and is common to printing processes that involve ink evaporation.^[25]

Electrical characterization was performed by measuring the sheet resistance of each sample using a four-probe method to eliminate contact resistances, as described in literature.^[5] Two probes were landed on each vapor-deposited silver pad and the current was swept from -100 to $100 \mu\text{A}$ between probes 1 and 2 while measuring the voltage between probes 3 and 4. The sheet resistance of each sample was measured before sintering, after sintering for 20 min at 150°C on the hotplate, and after flash sintering.

Sheet resistance is plotted as a function of withdrawal speed for the grids printed with $0.6 \mu\text{m}$ thick and $1.3 \mu\text{m}$ thick photoresists in **Figure 3a,b**, respectively. In addition to the marked increase in conductivity due to flash sintering as seen in

Figure 3b, two other trends promptly emerge. First, for both photoresists, sheet resistance increases with increasing withdrawal speed indicating a directly proportional relationship between the two. Second, for the same withdrawal speed, the thicker photoresist provides lower sheet resistance. Because the sheet resistance only depends on the grid thickness provided the line width is fixed, the results suggest that the grid thickness increases with a) decreasing withdrawal speeds, and b) the thickness of the photoresist used for patterning. The thickness dependence of the withdrawal speed in the evaporative regime for dipcoating is well studied.^[26] In the evaporative regime, increasing the withdrawal speed does not alter the evaporation rate at the meniscus but shortens the time window for particles to diffuse to the liquid adjacent to the substrate at the meniscus, which causes the number of particles getting deposited on the surface to decrease. The dependence of grid thickness on the photoresist thickness can be explained by geometrical confinement of the ink in lithographically defined channels. We hypothesize that some ink is trapped in the channels due to its interaction with the underlying substrate and the sidewalls of the photoresist, and the volume of the entrapped ink depends on the height of the sidewalls. Particles in the entrapped region have smaller diffusion distances to the air/substrate/ink interface than the particles in the bulk suspension. Thicker photoresist entraps a larger volume of ink (more particles with short diffusion distances), and thus provides thicker grids.

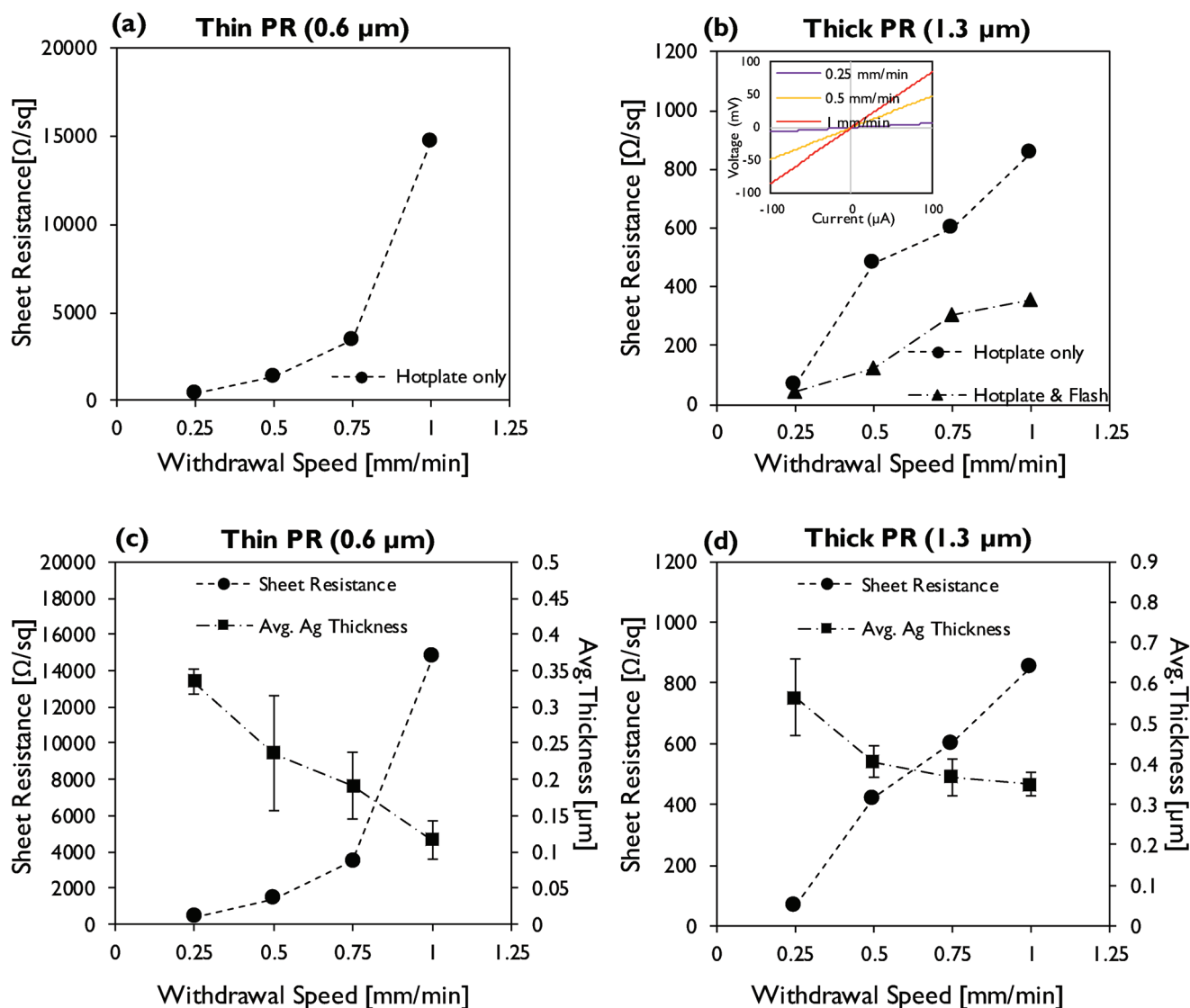


Figure 3. Sheet resistance versus withdrawal speed for 0.5 μm a) and 1.3 μm b) thick photoresists. The inset in (b) shows the *I*–*V* curves (hotplate only) showing linear behavior. The average thickness and sheet resistance for each withdrawal speed for 0.5 μm c) and 1.3 μm d) thick photoresists.

These hypotheses and observations were validated by comparing the average thickness of each sample measured by AFM imaging. Generally, the grids printed with the thicker PR and at slower withdrawal speeds were thicker and had lower sheet resistance values as shown in Figure 3c,d for 0.6 and 1.3 μm thick photoresists, respectively. However, two major anomalies were noticed: 1) the change in grid thickness is not linearly proportional to the change in sheet resistance, and 2) for comparable average thicknesses, the sheet resistance values for the two photoresists differed greatly. This suggests that the variation in electrical performance for different withdrawal speeds cannot solely be attributed to different grid thicknesses. Seemingly, at faster withdrawal speeds, not only the grid thickness decreases, but the packing density of the nanoparticles also decreases, which lessens the effectiveness of the subsequent sintering processes. Thus, the sheet resistance, even for comparable grid thicknesses, are smaller for the

thinner photoresist for slower withdrawal speeds. For instance, the grid electrode printed with 0.6 μm thick photoresist at 0.25 mm min^{−1} is about 300 nm thick and has a sheet resistance of the 367 Ω sq^{−1}. In contrast, the grid electrode printed with 1.3 μm thick photoresist at 1 mm min^{−1} is almost twice as thick but has a higher sheet resistance.

According to Kirchhoff's laws, the sheet resistance (*R_s*) of a grid electrode can be written as^[5]

$$R_s = \frac{N}{N+1} \frac{\rho L}{wt}$$

where *N* is the number of lines in the grid, *ρ* is the resistivity of bulk silver, *w* is the width of each line, *L* is the pitch, and *t* is the grid thickness. Using this relationship, theoretical sheet resistances of the printed grids were calculated and compared with the measured values. The average grid

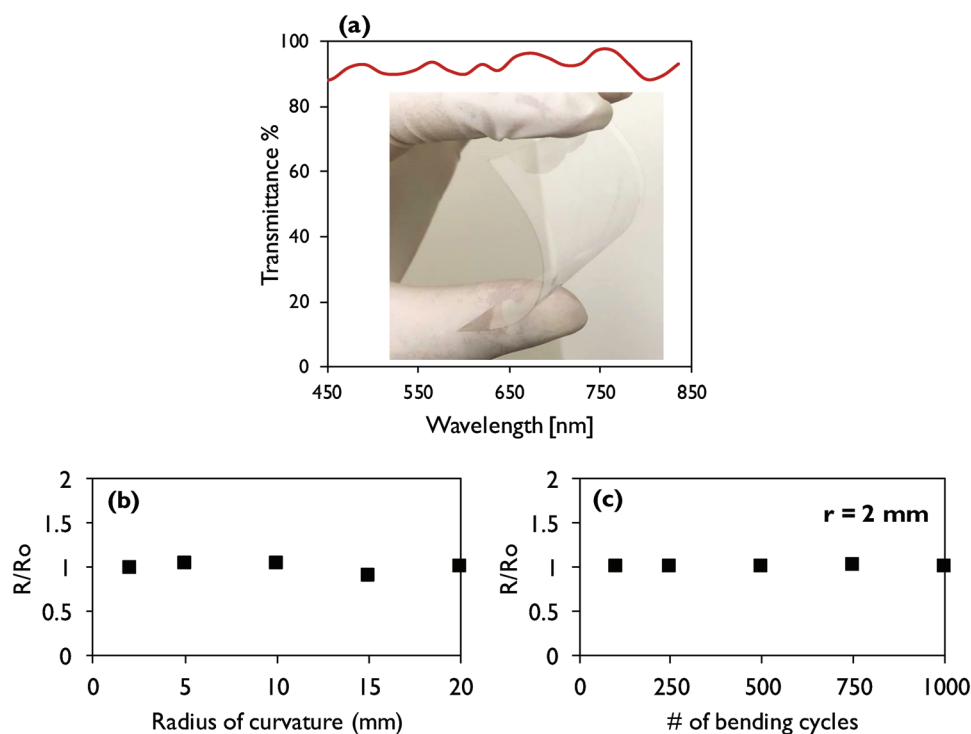


Figure 4. a) Optical transmittance of the grid electrode printed with sheet resistance of $43 \Omega \text{ sq}^{-1}$ ($1.3 \mu\text{m}$ thick photoresist, 0.25 mm min^{-1}). Change in resistance of the electrode due to bending to different radii of curvature for a single cycle b) and the change in resistance as a function of total bending cycles for 2 mm radius of curvature c).

thicknesses extracted from AFM measurements and the bulk resistivity of silver (1.59×10^{-8}) were used. The theoretical sheet resistances were found to be at least an order of magnitude smaller than the measured values. For example, the calculated sheet resistance of the grid printed using $1.3 \mu\text{m}$ thick PR at a withdrawal speed of 0.25 mm min^{-1} is about $0.8 \Omega \text{ sq}^{-1}$, which is about 47 times and 83 times smaller than the measured values of 43 and $67 \Omega \text{ sq}^{-1}$ for flash sintered and hotplate sintered samples, respectively. To put the sheet resistance data in a more realistic context, the sheet resistance of a vapor-deposited silver grid was compared to the sheet resistance of a printed sample with a similar average thickness and was found to be seven times smaller. The higher resistance of the printed samples can be attributed to charge scattering from interparticle boundaries, surfactant residue, and a few assembly defects (a few gaps or voids especially for higher withdrawal speeds). However, the sheet resistance is comparable to that attained using conventional printing techniques while providing better optical transmission due to the smaller line width.

The optical transmittance of the grid electrode was experimentally determined using an in-house built tool in the wavelength range of 400–900 nm. A tradeoff between optical transmittance and sheet resistance exists due to obvious physical constraints. Increasing line width increases conductivity but lowers optical transmittance as wider lines reflect more light. This is defined by the relationship between optical transmittance and the fill factor (f) that represents the ratio of the area covered by the grid lines to the total substrate area independent of the grid thickness.^[14] The f for the designed grid with a line width of $2 \mu\text{m}$

and a pitch of $100 \mu\text{m}$ is fixed at 0.04 for all samples and hence, measuring the transmittance of a single sample should suffice. For this reason, the transmittance of the sample with the highest sheet resistance ($43 \Omega \text{ sq}^{-1}$, $1.3 \mu\text{m}$ thick photoresist, 0.25 mm min^{-1}) was measured and divided by the transmittance of a blank PET sample. The average transmittance in the visible light range (450–750 nm) is above 92% and peaks at around 96% around 700 nm as shown in Figure 4a. This transmittance along with a sheet resistance of $43 \Omega \text{ sq}^{-1}$ is well suited to most optoelectronic applications. However, the tradeoff between withdrawal speed and sheet resistance for different photoresist thicknesses can be explored to tailor electrodes for various purposes. For instance, solar cells typically require a sheet resistance of less than $50 \Omega \text{ sq}^{-1}$ to avoid undesired power loss from joule heating,^[27] for which electrodes printed at low speeds with thicker photoresists are suitable. However, for applications such as large displays and field effect devices where a sheet resistance of up to $1000 \Omega \text{ sq}^{-1}$ is acceptable,^[28] a higher pulling speed and thinner photoresists may be employed.

A major drawback of ITO is its brittleness, and any suggested alternatives should ideally demonstrate high flexibility with a minimal loss in conductivity. To explore this aspect, a grid electrode printed with $1.3 \mu\text{m}$ thick photoresist at 0.25 mm min^{-1} was bent post hotplate and flash sintering to different radii of curvature between 2 and 20 mm for a single cycle, and the change in its resistance, R/R_0 , was quantified. As shown in Figure 4b, no significant change in the resistance occurred and R/R_0 remained stable around 1.0 even for very small radii. Some emerging photoelectronic applications such as foldable screens may also require the transparent electrode

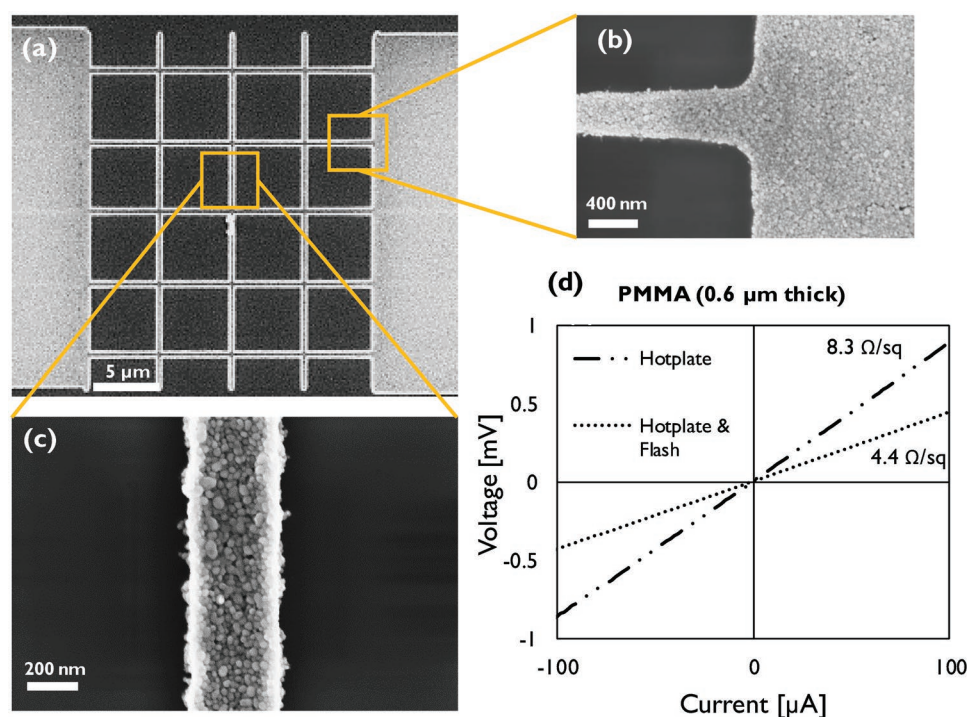


Figure 5. SEM micrographs of the nanoscale grid printed on a glass wafer through e-beam lithography are shown in (a)–(c). The I – V characteristics of the same electrode for difference sintering processes are shown in (d).

to undergo many bending cycles without a significant change in its resistance. To characterize the suitability of the proposed electrode for such applications, the fatigue characteristics were tested by subjecting a hotplate and flash sintered grid electrode to 1000 cycles of bending to 2 mm radius of curvature and quantifying the ratio R/R_0 every 250 cycles. Interestingly, negligible change (less than 5%) in sheet resistance was seen over 1000 cycles as shown in Figure 4c. The results indicate good adhesion between the printed and sintered silver and the PET substrate.

The capability to print nanoscale features is demonstrated by patterning an ≈ 0.6 μm thick PMMA layer spin-coated on glass with a grid of 300 nm line width and 5 μm pitch using electron beam lithography. Glass was chosen as the substrate to facilitate the patterning process but the same can be achieved on a flexible substrate. Two large pads (50 μm × 25 μm) were patterned on either side of the grid to facilitate its electrical characterization. The withdrawal speed was set at 0.07 mm min⁻¹ as the large pads also needed to be filled alongside nanoscale features. SEM micrographs of the printed grid with nanoscale line width are shown in Figure 5a–c. The sheet resistance was found to be ≈ 5 Ω sq⁻¹ after hotplate and flash sintering, which is only seven times higher than the theoretical value of about 0.7 Ω sq⁻¹. The improved electrical behavior of nanoscale grid is because fewer printing defects occur over a significantly smaller area. Moreover, slower withdrawal speeds provide better packing of particles thereby increasing conductivity.

In summary, a versatile method for printing high-resolution grid electrodes for high resolution display and touch display applications at room temperature at a low cost. The electrode

properties can be tailored for various applications by tuning the printing process. The presented process is scalable as many large-sized substrates can be printed simultaneously. The presented grid electrode with a sheet resistance of 43 Ω sq⁻¹ with an average transmittance of over 92% can potentially replace ITO or vapor-deposited grid electrodes for most applications. The process can be further improved by utilizing a higher quality nanoparticle ink, better sintering processes, and the use of patterning tools specialized for flexible substrates. Overall, this additive technique provides a promising method for industrial scale printing of metal grid electrodes for current and emerging applications.

Experimental Section

Materials: Silver nanoparticle ink (JS101A 40 wt% in diethylene glycol) was obtained from NovaCentrix with 50 nm roughly spherical particles. PET (Melinex 454) was obtained from Dupont Teijin. Silver ink was diluted to 2 wt% using 18 MΩ deionized water. For assembly, a KSV Systems dipcoater was used inside a desiccated chamber with humidity at <20%.

Fabrication Process: To prepare each sample, a 4 in. wafer was cut out of the PET film and treated with RF generated oxygen plasma at 115 W for 2 min (Anatech 100, gas flow 15 sccm, pressure 0.38 Torr) to clean the film of any organics and to make its surface hydrophilic. The PET substrate was then patterned using photolithography (Quintel 4000) with a square grid 5 cm × 5 cm in size with a line width of 2 μm and pitch of 100 μm. Two different PRs, S1805 (0.5 μm thick) and S1813 (1.3 μm thick), were spun at 4000 RPM for 45 s followed by exposure and development (AZ 726). The back of the PET substrate was also coated with Shipley S1813 and baked for 30 s at 115 °C to avoid assembly on the backside.

For characterization, 1.25 cm wide, 5 cm long and 100 nm thick silver electrodes were deposited at the edge of each flexible substrate using a shadow mask via electron beam evaporation. Each substrate was then cut precisely into half to create two perfect 2.5 cm × 2.5 cm squares. A 2.5 cm × 2.5 cm area served as the test electrode. For electrical characterization, sheet resistance of both squares was measured. Negligible difference ($\approx 10 \Omega \text{ sq}^{-1}$) was found between two squares cut out from each sample indicating uniform printing of silver over 5 cm × 5 cm area. The schematic for the process is shown in the Supporting Information.

For the nanoscale grid, a glass wafer was plasma cleaned as previously described and coated with ≈ 600 nm thick layer of poly (methyl methacrylate) (PMMA). The wafer was then baked at 100 °C for 30 min on hotplate. The pattern was written using a 60 μm aperture (Carl Zeiss Supra 25, NPGS). The wafer was developed using a 3:1 (IPA:MIBK) mixture for 80 s. The withdrawal speed was set as 0.07 mm min⁻¹ to simultaneously print the larger pads to assist electrical characterization.

Dipcoating-Based Assembly Process: Dipcoating-based directed assembly of silver nanoparticles was used to fill the patterned trenches with silver. Humidity in the environment for maintained at 20% using a desiccated cabinet. After assembly, the photoresist was removed by gently rinsing the substrates in acetone and isopropyl alcohol for 2 min each, respectively.

Sintering: The samples were stacked between the polished sides of two clean silicon wafers before being placed on the hotplate to avoid contamination and to keep the film unwrinkled. For flash sintering a Novacentrix 1300 flash sintering system was used at 300 V in a multipulse mode under nitrogen.

Characterization: The morphology of the silver grid was studied using a Zeiss Supra 25 SEM. The morphology and the thickness of the printed silver lines was measured using an NX-20 Park Systems AFM and a Zeiss Smartproof 5 confocal microscope, respectively. For confocal microscopy, a 50× objective was used to stitch a 500 μm × 500 μm area containing four to five printed lines in each direction. The cross-section profile of the captured lines was then extracted, and the mean height was determined along with the standard deviation. An example is shown in Figure S2 (Supporting Information) for the grid printed at 0.25 mm min⁻¹ using the 1.3 μm thick photoresist.

Electrical characterization on the square substrates was performed using an Agilent 4156C system and a Summit Cascade 12000 probe station with DCP-HTR 19 μm probe tips in a four-probe configuration. Optical characterization was done using a custom-built tool with a white light source of 400 W. Mechanical performance was evaluated by cutting circular pathways of fixed radii in a plastic sheet and bending the electrode to match the radii.

Supporting Information

Supporting Information is available from the Wiley Online Library or from the author.

Acknowledgements

The experiments were conducted at the Georg J. Kostas Nanoscale Technology and Manufacturing Research Center. The authors acknowledge support from the Massachusetts Technology Collaborative. The authors also thank Aidan Gould for help with confocal microscopy.

Conflict of Interest

The authors declare no conflict of interest.

Keywords

display, flexible, printed electronics, silver grid, transparent electrodes

Received: May 21, 2019

Revised: June 25, 2019

Published online: August 9, 2019

- [1] M. H. Frey, L. Zu, E. S. Hagermoser, *US Patent Application 0219257*, **2012**, <https://link.springer.com/article/10.1007/s00170-013-4907-z>.
- [2] Y. Liu, S. Shen, J. Hu, L. Chen, *Opt. Express* **2016**, *24*, 25774.
- [3] Y. Li, L. Mao, Y. Gao, P. Zhang, C. Li, C. Ma, Y. Tu, Z. Cui, L. Chen, *Sol. Energy Mater. Sol. Cells* **2013**, *113*, 85.
- [4] J. Park, J. Lee, Y.-Y. Noh, *Org. Electron.* **2012**, *13*, 184.
- [5] J. van de Groep, P. Spinelli, A. Polman, *Nano Lett.* **2012**, *12*, 3138.
- [6] D. S. Ghosh, T. L. Chen, *Appl. Phys. Lett.* **2010**, *96*, 041109.
- [7] H.-J. Choi, S. Choo, P.-H. Jung, J.-H. Shin, Y.-D. Kim, H. Lee, *Nano-technology* **2015**, *26*, 055305.
- [8] P. Rajesh Desai, P. Nikhil Desai, K. Deepak Ajmera, K. Mehta, *Int. J. Eng. Trends Technol.* **2014**, *13*, 175.
- [9] Y. H. Kahng, M.-K. Kim, J.-H. Lee, Y. J. Kim, N. Kim, D.-W. Park, K. Lee, *Sol. Energy Mater. Sol. Cells* **2014**, *124*, 86.
- [10] J. H. Park, D. Y. Lee, Y.-H. Kim, J. K. Kim, J. H. Lee, J. H. Park, T.-W. Lee, J. H. Cho, *ACS Appl. Mater. Interfaces* **2014**, *6*, 12380.
- [11] Y. Huang, X. Bai, M. Zhou, S. Liao, Z. Yu, Y. Wang, H. Wu, *Nano Lett.* **2016**, *16*, 5846.
- [12] L. Hu, H. S. Kim, J.-Y. Lee, P. Peumans, Y. Cui, *ACS Nano* **2010**, *4*, 2955.
- [13] K. Dong Jin, L. Mikyung, S. L. Seung, K. Jin-Ha, *AIP Adv.* **2017**, *7*, 105218.
- [14] Y.-Y. Zhao, M.-L. Zheng, X.-Z. Dong, F. Jin, J. Liu, X.-L. Ren, X.-M. Duan, Z.-S. Zhao, *Appl. Phys. Lett.* **2016**, *108*, 221104.
- [15] S. De, T. M. Higgins, P. E. Lyons, E. M. Doherty, P. N. Nirmalraj, W. J. Blau, J. J. Boland, J. N. Coleman, *ACS Nano* **2009**, *3*, 1767.
- [16] Y. Jang, J. Kim, D. Byun, *J. Phys. D: Appl. Phys.* **2013**, *46*, 155103.
- [17] Z. Xin, Y. Liu, X. Li, S. Liu, Y. Fang, Y. Deng, C. Bao, L. Li, *Mater. Res. Express* **2017**, *4*, 015021.
- [18] N. E. Hjerrild, D. C. J. Neo, A. Kasdi, H. E. Assender, J. H. Warner, A. A. R. Watt, *ACS Appl. Mater. Interfaces* **2015**, *7*, 6417.
- [19] M. M. Falinski, D. L. Plata, S. S. Chopra, T. L. Theis, L. M. Gilbertson, J. B. Zimmerman, *Nat. Nanotechnol.* **2018**, *13*, 708.
- [20] C. Yang, J. Kim, *Indian Acad. Sci.* **2018**, *41*, 1.
- [21] a) C. J. Brinker, in *Chemical Solution Deposition of Functional Oxide Thin Films* (Eds: T. Schneller et al.), Springer, London **2013**, p. 233; b) P. Born, S. Blum, A. Munoz, T. Kraus, *Langmuir* **2011**, *27*, 8621.
- [22] a) R. R. A. Syms, E. M. Yeatman, V. M. Bright, G. M. Whitesides, *J. Microelectromech. Syst.* **2003**, *12*, 387; b) J. M. K. Ng, M. J. Fuerstman, B. A. Grzybowski, H. A. Stone, G. M. Whitesides, *J. Am. Chem. Soc.* **2003**, *125*, 7948.
- [23] S. Ni, L. Isa, H. Wolf, *Soft Matter* **2018**, *14*, 2978.
- [24] a) X. Xiong, L. Jaberansari, G. Hahm Myung, A. Busnaina, J. Jung Yung, *Small* **2007**, *3*, 2006; b) L. Jaber-Ansari, M. Hahm, T. Kim, S. Somu, A. Busnaina, Y. Jung, *Appl. Phys. A: Mater. Sci. Process.* **2009**, *96*, 373.
- [25] a) W. Su, B. S. Cook, Y. Fang, M. M. Tentzeris, *Sci. Rep.* **2016**, *6*, 35111; b) X. Zhong, A. Crivoi, F. Duan, *Adv. Colloid Interface Sci.* **2015**, *217*, 13.
- [26] a) S. Roland, C. G. Gamys, J. Grosrenaud, S. Boissé, C. Pellerin, R. E. Prud'homme, C. G. Bazuin, *Macromolecules* **2015**, *48*, 4823; b) L. Cisneros-Zevallos, J. Krochta, *J. Food Sci.* **2003**, *68*, 503.
- [27] G. Willeke, E. R. Weber, *Advances in Photovoltaics: Part 3*, Vol. 90, Academic Press, Amsterdam **2014**.
- [28] A. Piegari, F. o. Flory, *Optical Thin Films and Coatings: From Materials to Applications*, Woodhead Publishing, Philadelphia, PA **2013**.